



# Tailored synthesis of active reduced graphene oxides from waste graphite: Structural defects and pollutant-dependent reactive radicals in aqueous organics decontamination

Yuxian Wang<sup>a,b</sup>, Hongbin Cao<sup>a</sup>, Lulu Chen<sup>c</sup>, Chunmao Chen<sup>b</sup>, Xiaoguang Duan<sup>d</sup>, Yongbing Xie<sup>a,\*</sup>, Weiyu Song<sup>c,\*</sup>, Hongqi Sun<sup>e</sup>, Shaobin Wang<sup>d</sup>

<sup>a</sup> Division of Environment Technology and Engineering, Institute of Process Engineering, Chinese Academy of Sciences, Beijing, 100190, China

<sup>b</sup> State Key Laboratory of Heavy Oil Processing, Department of Chemical Engineering, China University of Petroleum, 18 Fuxue Road, Beijing, 102249, China

<sup>c</sup> State Key Laboratory of Heavy Oil Processing, College of Science, China University of Petroleum, 18 Fuxue Road, Beijing, 102249, China

<sup>d</sup> Department of Chemical Engineering, Curtin University, GPO Box U1987, Perth, Western Australia, 6845, Australia

<sup>e</sup> School of Engineering, Edith Cowan University, 270 Joondalup Drive, Joondalup, Western Australia 6027, Australia

## ARTICLE INFO

### Keywords:

Reduced graphene oxide  
Catalytic ozonation  
Defects  
Density functional theory  
Reactive oxygen species

## ABSTRACT

Anode graphite was recovered from a spent lithium ion battery (LIB) and reutilized as a carbon precursor to obtain graphene-based materials. Characterization results revealed that impurities were removed from the obtained graphite powder by cleansing processes. The as-synthesized reduced graphene oxide (rGO) from the purified graphite (LIB-rGO) demonstrated excellent catalytic ozonation activity against organic pollutants removal. To probe potential catalytic active sites, LIB-rGOs with different defective levels but similar oxygen contents were synthesized. Catalytic ozonation tests revealed that a higher defective level resulted in a greater catalytic activity. Density functional theory (DFT) calculation further demonstrated that ozone molecules could spontaneously decompose into active oxygen species on graphene structural vacancies and edges, which consolidated the role of defective structure in catalytic ozonation activity. Meanwhile, we discovered the pollutant-structure-dependent behavior of dominant reactive oxygen species (ROS) with the aid of radical scavenging tests and electron paramagnetic resonance (EPR) spectra. For phenolic pollutants vulnerable to direct ozone attacking, superoxide radicals ( $O_2^{\cdot-}$ ) and singlet oxygen ( $^1O_2$ ) were found to be responsible ROS, whereas hydroxyl radicals ( $\cdot OH$ ) were identified as the principle ROS for aliphatic organic pollutants destruction. This study not only put forward a possible way for reutilization of waste LIB anode, but also stepped further for investigating the catalytic ozonation mechanism towards the graphene-based materials including the active sites and the generation of ROS.

## 1. Introduction

Advancing in industrialization and civilization of human society has brought great challenges in environmental remediation, especially the water contamination [1]. Persistent organic pollutants (POPs) such as phenolic compounds and organic acids discharged from oil/coal processing wastewater and municipal sewage place detrimental effects to human health and the ecosystem. Great research interests have been aroused to seek for the effective removal technologies of these POPs [2–4]. Advanced oxidation processes (AOPs) with the generated active radicals become the hotspot due to their fast reaction rates with organics and complete mineralization capability [5–7]. Compared with ozonation process, catalytic ozonation is a more efficient AOP for non-

selective mineralization of aqueous organic pollutants, relying on the generated reactive oxygen species (ROS) as well as the ozone molecules [8,9].

Metal-based catalysts have been proved to be highly reactive in catalytic ozonation, however, the deactivation by metal leaching cannot be fully avoided [10]. To construct a sustainable future, the emerging carbon-based materials, especially nanocarbons, have been developed as the state-of-the-art alternatives to the metal-based materials for environmental catalysis due to their exceptional physico-chemical properties, no heavy metal leaching and environmental friendliness [5,11–15]. Studies revealed that graphene oxide (GO) and reduced graphene oxide (rGO) materials demonstrated excellent catalytic ozonation activities in destruction of POPs [8,16]. Defects, surface oxygen

\* Corresponding authors.

E-mail addresses: [ybxie@ipe.ac.cn](mailto:ybxie@ipe.ac.cn) (Y. Xie), [songwy@cup.edu.cn](mailto:songwy@cup.edu.cn) (W. Song).

containing groups have been speculated to be the potential active sites. Our previous work revealed that surface oxygen containing groups, especially the carbonyl groups would contribute to the catalytic efficiency [8]. However, the in-depth insights into the contribution of these potential active sites within rGO to the catalytic ozonation still remain unveiled. On the other hand, the agreement of the dominant reactive species for different organic pollutants mineralization has not been reached [17–19]. Recently, non-hydroxyl radical dependent pollutants degradation pathways were discovered for phenolic pollutants degradation [4,19,20]. It is plausible that the dominant ROS are relevant with the structures of the target pollutants. Unveiling the relationship between the target pollutants and the generated ROS would step further for probing the catalytic ozonation mechanism.

Recently, various types of carbonaceous waste which are rich in carbon content, low cost, and natural abundance have been reutilized for synthesis of carbon-based functional materials with tunable surface chemistry and structures [21]. Efficient catalysis utilizing these carbonaceous waste for hydrogen production [22,23], cathodic oxygen reduction reaction (ORR) [24,25] and water remediation [26,27] has been achieved, and a sustainable material cycling towards green catalysis has been created. Most of the carbonaceous materials are derived from waste biomass, however, utilization of the anode graphite from spent lithium ion batteries (LIBs), which is of great abundance due to their limited life span, is very limited [28,29]. Therefore, recycling the waste graphite from spent LIBs to synthesize an active graphene-based catalyst for contaminated water treatment is desirable to solve both the environmental and energy issues.

In this study, we recovered the graphite from a spent LIB via a facile method and utilized it as the precursor for synthesizing a series of graphene-based materials by thermal, hydrothermal and chemical reduction, respectively. The activities of the as-prepared materials were evaluated in catalytic ozonation of oxalic acid (OA), one of well-recognized terminal products for organic pollutant destruction. Relationship between the defective level and the catalytic activities was then investigated. DFT calculation was performed to provide the insights into the active sites for catalytic ozone decomposition. In order to evaluate the influence of target pollutant structures on the generated dominated ROS, three aliphatic organics, i.e. OA, acetic acid (AA) and formic acid (FA) and three phenolic pollutants, i.e. 4-nitrophenol (4-NP), para-hydroxyl benzoic acid (PHBA) and acetylsalicylic acid (ASA) were selected as the target organics. Electron paramagnetic resonance (EPR) tests with radical scavenging tests were then performed to examine the ROSs. This study provides a painstaking envisage on the mechanism of graphene-based materials catalytic ozonation.

## 2. Experimental

### 2.1. Chemicals and materials

Formic acid (99.5%), acetic acid (99.5%), oxalic acid (99.5%), tert-butanol (t-BA, 99.0%), sodium azide ( $\text{NaN}_3$ , 99.0%) and hydrogen peroxide (30%) were obtained from Sinopharm Chemical Reagent Co. Ltd. Acetylsalicylic acid (99.9%), para-hydroxyl benzoic acid (PHBA, 99.9%), 4-nitrophenol (99.9%), and *N,N*-dimethylformamide (DMF, 99.5%) were purchased from Aladdin Reagent. Nitric acid (70%), sulfuric acid (98%) and potassium permanganate (99.5%) were purchased from Beijing Chemical Plant, China. 5,5-Dimethyl-1-pyrroline (DMPO) and 2,2,6,6-tetramethyl-4-piperidone (TEMP) were procured from Sigma-Aldrich. 5-tert-Butoxycarbonyl-5-methyl-1-pyrroline-*N*-oxide (BMPO) were purchased from DOJINDO, Japan. Commercial graphite powder (250 mode) (99.99%) was obtained from Alfa Aesar. Horseradish peroxidase (POD, specific activity of  $> 250 \text{ u mg}^{-1}$ ) was obtained from Amresco (USA). All chemicals were of analytical grade and used without further purification. The pH of solutions was adjusted by diluted NaOH and HCl solutions.

### 2.2. Synthesis of the graphene based materials

The spent anode graphite was purified by acid/alkaline wash and water/ethanol wash. The detailed purification process was described in Text S1 in Supplementary data. Graphene oxide (GO) was prepared by a modified Hummers' method from LIB-Graphite and denoted as LIB-GO [30]. The detailed preparation route can be found in Text S2 in Supplementary data. For the synthesis of rGO, LIB-GO (1 g) was transferred into a capped crucible and heated in an airtight muffle furnace at  $80^\circ\text{C}$  for 1 h, followed by heating at  $300^\circ\text{C}$  for another 1 h and denoted as LIB-rGO. A commercial graphite powder was treated using the same procedure and the product was marked as C-rGO. For comparison, another two rGO samples were prepared from chemical reduction method [31] and hydrothermal method [6] from the LIB-GO sample and labelled as LIB-rGO-C and LIB-rGO-H, respectively.

### 2.3. Characterization methods

X-ray diffraction (XRD) patterns (X'Pert-PROMPD, PAN analytical B.V.);  $\text{N}_2$  sorption isotherms (Autosorb-iQ, Quantachrome); Field emission scanning electron microscope (FESEM, JSM-7001F); Transmission electron microscopy (TEM, JEOL 2100F); X-ray photoelectron microscopy (XPS, Thermo Fisher Scientific ESCALAB 50Xi); Raman spectra (Renishaw inVia); Electron spin resonance (EPR, Bruker EMX) were employed for characterization of the catalysts and the relevant processes. The detailed description of the characterization methods could be found in Text S3 in supplementary data.

### 2.4. Experimental procedures

Ozonation and catalytic ozonation experiments were conducted in a semi-batch reactor containing 0.5 L of the solution at  $25^\circ\text{C}$ . In a typical experiment, the catalyst (0.1 g/L) was dosed into the reactor under stirring with a speed of 300 rpm for 15 min to achieve adsorption-desorption equilibrium. Ozone was produced by an ozone generator (Anseros Ozomat GM) from high purity oxygen (99.99%) with an inlet flow rate of 100 mL/min. The concentration of gaseous ozone was 50 mg/L, monitored by an ozone detector (Anseros Ozomat GM), and it was bubbled into the bottom of the reaction through a porous diffuser. At given time intervals, samples were withdrawn from the reactor and filtered by a  $0.22 \mu\text{m}$  PTFE filter for further analysis. The filtrate was analyzed by a high performance liquid chromatography (HPLC, Agilent Series 1260) using a C-18 column at a flow rate of 0.25 mL/min. The mobile phases were a mixture of diluted phosphate acid and methanol for OA, FA, AA, PHBA and 4-NP analysis, and a mixture of ultrapure water and methanol for ASA analysis.

### 2.5. Theoretical calculation methods

Density functional theory (DFT) calculations performed with the Vienna Ab-initio Simulation Package (VASP) using Perdew-Burke-Ernzerhof (PBE) for exchange correlation energy with a semi-empirical van der Waals (vdW) correction to account for dispersion interaction were applied to investigate the chemisorption of ozone on graphene surface. The detailed description of DFT calculation can be found in Text S4 in Supplementary data.

## 3. Results and discussion

### 3.1. Characterization of catalysts

XRD patterns revealed that a hexagonal crystal structure ( $\text{P6}_3/\text{mmc}$ ) with a sharp peak centered at  $26.7^\circ$  was identified (JCPDS No. 00-008-0415) for LIB-Graphite (Fig. S1(A)), indicating a well-defined ordered graphite structure with high crystallinity [32]. No discernable peaks for Li, Mn, Co and Ni or their oxides were observed, which suggested that

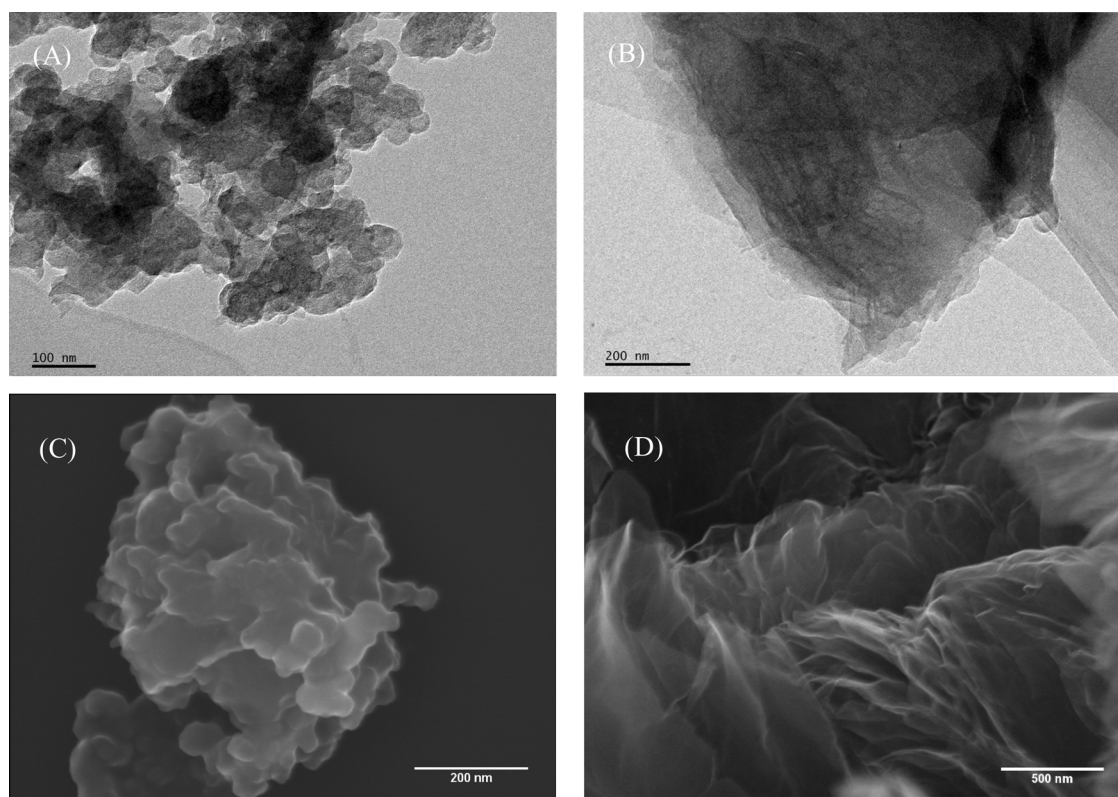


Fig. 1. TEM image of LIB-Graphite (A) and LIB-rGO (B); SEM images of LIB-Graphite (C) and LIB-rGO (D).

metal impurities were completely removed during material synthesis [33]. The broad peak centered at  $24.6^\circ$  revealed the formation of disordered reduced graphene oxides on LIB-rGO [6]. To compare, the XRD patterns of commercial graphite and the corresponding rGO were listed in Fig. S1(B).

The morphologies of the as-synthesized graphene-based materials are shown in Fig. 1. For LIB-Graphite (Fig. 1(A) and (C)), stacked flakes with a radius between 50 and 100 nm were observed. SEM images suggested that LIB-GO (Fig. S2(B)) with wrinkled silk-like structure and the highly exfoliated LIB-rGO (Fig. 1(B)) were synthesized, the morphologies of which are quite in accordance with the previously reported ones [8,34]. The EDX elemental mappings suggested that the high purity of the obtained graphene-based materials (Fig. S2). Only trace of Si ( $\leq 0.4$  wt.%) remained (Table S1). This was further confirmed with TGA results (Fig. S3) that less than 0.3 wt.% of fresh samples were remained in LIB-Graphite, LIB-GO and LIB-rGO after high temperature pyrolysis in air.

XPS survey suggested that LIB-GO obtained the highest oxygen level of 26.3 at.%, due to the grafting of various oxygen functional groups during the oxidation process (Table S2). The heat reduction eliminated oxygen functional groups and the oxygen level of LIB-rGO decreased to 17.2 at. %. High resolution C1s scan (Fig. S5) further revealed that most of the ketonic and carboxylic groups on LIB-GO were removed after heat reduction, while the remaining was reduced into hydroxyl/epoxy groups on LIB-rGO. On the other hand, thermal explosion and exfoliation of solidly stacked graphene layers within LIB-GO enormously enlarged the specific surface area and pore volume of LIB-rGO from 49.6 to 362.4  $\text{m}^2/\text{g}$  and 0.09 to 0.92  $\text{cm}^3/\text{g}$ , respectively (Table 1).

On the other hand, the reduction process also created defective sites by transforming the  $\text{sp}^2$  carbons to  $\text{sp}^3$  carbons, resulting in the collapse of the carbon skeleton and reformation of defective edges [35]. Compared with LIB-GO, the composition of  $\text{sp}^3$  carbons within graphene basal plane in LIB-rGO increased from 10.95 at. % to 14.52 at. % (Table 1), suggesting more disordered structure was formed. This

Table 1  
Surface chemistry properties of as-synthesized samples.

Sample	$S_{\text{BET}}$ ( $\text{m}^2/\text{g}$ )	Pore volume $\text{cm}^3/\text{g}$	Carbon species		Oxygen species (based on C1s scan)		
			$\text{sp}^2$ carbon (%)	$\text{sp}^3$ carbon (%)	C–O–C/ C–OH (at. %)	C=O (at. %)	O–C=O (at. %)
LIB-Graphite	36.2	0.10	44.00	36.18	9.46	4.81	4.8
LIB-GO	49.6	0.09	56.45	10.95	6.37	15.78	10.17
LIB-rGO	362.4	0.92	64.55	14.52	10.2	3.31	6.60
LIB-rGO-H	394.7	0.83	50.68	29.39	10.14	2.29	7.14
LIB-rGO-C	370.1	0.82	51.26	25.66	12.94	4.45	4.69
C-rGO	335.3	1.26	64.00	11.43	12.61	4.19	7.77

variation in defective sites was further validated by Raman spectra (Fig. 2). LIB-rGO obtained a higher  $I_{\text{D}}/I_{\text{G}}$  than LIB-GO (0.93 vs. 0.81) due to the transformation from  $\text{sp}^2$  carbon to  $\text{sp}^3$  carbon by thermal annealing.

### 3.2. Catalytic ozonation of oxalic acid

Pollutants degradation profiles using the as-prepared materials are depicted in Fig. 3. OA was employed as the target pollutant in catalytic ozonation/ozonation processes due to its inertness against the direct attacking of ozone molecule [36,37]. As expected, less than 10% of OA was removed in ozonation. Moreover, the adsorption of OA on the as-synthesized graphene-based materials was negligible (Fig. 3(A) and (C)). Within the acid environment ( $\text{pH} = 3.0$ ), OA mainly presented in the form of  $\text{HC}_2\text{O}_4^-$  as a weak acid with  $\text{pK}_{\text{a}1} = 1.2$  and  $\text{pK}_{\text{a}2} = 4.2$ . Owing to the lower point of zero charge ( $\text{pH}_{\text{pzc}}$ ) values of the LIB-Graphite, LIB-rGO and LIB-GO (2.1, 2.8 and 2.6, respectively) than the solution pH (3.0), the expelling force between the catalyst surfaces and the OA molecules resulted in insignificant physical adsorption (Fig. 3(B)). Nevertheless, around 40% of OA adsorption was observed



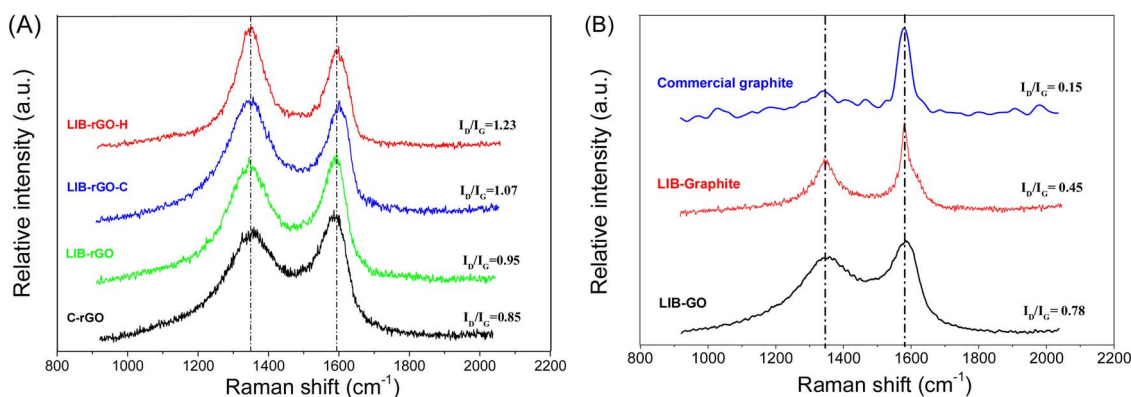


Fig. 2. (A) Raman spectra of C-rGO, LIB-rGO, LIB-rGO-C and LIB-rGO-H; (B) Raman spectra of reference commercial graphite, LIB-Graphite and LIB-GO.

on a commercial graphite arising from its electropositive surface ( $\text{pH}_{\text{pzc}} = 4.4$ ).

In terms of catalytic ozonation, a commercial graphite was employed as the benchmark. As seen, less than 60% of the OA was degraded after 1 h reaction, which was slightly higher than that in adsorption, indicating its deficient capability in ozone activation. C-rGO accomplished 95% OA removal within 1 h, while LIB-rGO demonstrated a higher catalytic activity and complete OA degradation was achieved in 45 min. As seen in Fig. 3(B), commercial graphite displayed a poor catalytic activity, while LIB-Graphite demonstrated somewhat catalytic ozonation activity leading to a 70% removal of oxalic acid at 60 min. Compared with commercial graphite obtaining the  $I_D/I_G$  ratio of 0.15 (Fig. 2(B)), this recovered LIB-Graphite from waste anode possessed a greater  $I_D/I_G$  ratio of 0.45 which might derive from the purification processes. And the higher defective level resulted in an increased catalytic activity. However, its catalytic activity was much inferior to those of LIB-rGO and C-rGO, which obtaining much higher  $I_D/I_G$  ratios and

achieved complete oxalic acid degradation in 45 min. Effects of OA concentration and LIB-rGO dosage to catalytic ozonation were also investigated (Fig. S6 and S7). General trends could be observed that higher pollutant concentration resulted in lower degradation efficiency, while increase the catalyst dosage could remarkably elevate the OA degradation rate. To evaluate the reaction rate, a first-order reaction kinetics was fit for the degradation curves (Fig. 3(D) and Table S3).

The surface structural vacancies and edges constituting the defects within rGO structure have also been reported as the potential active site in nanocarbons catalysis, because the delocalized electrons could modulate various properties of rGO, such as surface reactivity, mobility of adsorbed species and electron conductivity [12,38–40]. Surface oxygen functional groups on rGO are also widely recognized as the critical active sites within carbocatalysis [41,42]. In this system, LIB-rGO with lower specific surface area possessed even higher activity than C-rGO (Fig. 3(A)). LIB-rGO and C-rGO had a similar composition of the oxygen functional groups, yet the defective level differed (Fig. 3).

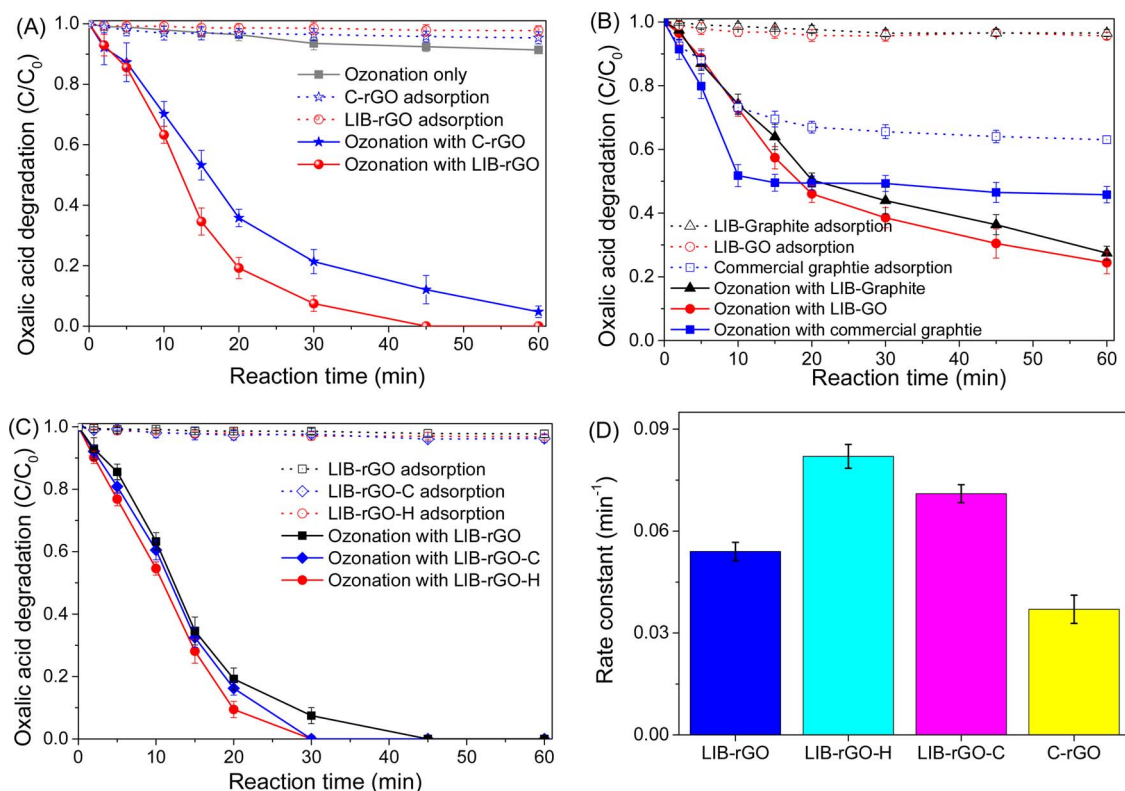


Fig. 3. (A) OA removal in ozonation, adsorption and catalytic ozonation with different materials; (B) OA adsorption and degradation over different LIB-rGO materials; (C) OA adsorption and degradation over various materials; (D) Reaction rate constant for LIB-rGO made from different methods in OA degradation.  $[\text{OA}]_0$ : 50 mg/L, Catalyst loading: 0.1 g/L, Ozone flow rate: 100 mL/min, Ozone concentration: 50 mg/L, Temperature: 25 °C, Initial pH: 3.0.

Therefore, we speculate the higher defective level of LIB-rGO might play a crucial role in activation of ozone molecules.

To further investigate the effect of structural defects on the catalytic activity, we synthesized another two rGOs materials from LIB-GO, i.e. LIB-rGO-C and LIB-rGO-H, by chemical reduction and hydrothermal reduction, respectively. In Table 1, LIB-rGO, LIB-rGO-C and LIB-rGO-H have a similar level of oxygen content (17.2 at.%, 15.3 at.% and 16.4 at.%, respectively) and composition of oxygen species, yet a large deviation in the amount of  $sp^3$  carbon (14.5 at.%, 25.7 at.% and 29.4 at.%, respectively). The difference in the ratio of  $sp^3$  carbon indicated that rGO prepared from hydrothermal reduction obtained the highest structural disordered level on the graphene basal plane, while heat reduced rGO showed the lowest level of structural disorder. This trend was further confirmed by Raman spectra in Fig. 2(A). The  $I_D/I_G$  ratios for LIB-rGO, LIB-rGO-C and LIB-rGO-H were 0.93, 1.05 and 1.25, respectively. The sequence of  $I_D/I_G$  was in well agreement with the proportion of  $sp^3$  carbon, and the defective degree is in the order of LIB-rGO-H > LIB-rGO-C > LIB-rGO. The reactivity of these three rGO samples was compared in catalytic ozonation of OA (Fig. 3(C)). It was found that the catalytic activity was directly influenced by the defects, and a higher defective level gave rise to a better catalytic activity in OA decomposition. Specifically, the first-order reaction rate constant over LIB-rGO-H with the highest defect level was greater than that over LIB-rGO with the lowest defect level (Fig. 3(D) and Table S3). On the other hand, the larger specific surface area of LIB-rGO-H also provided more active sites. Therefore, we postulate that structural defects (i.e. vacancies and defective edges) on rGO are the main active sites for ozone activation.

### 3.3. Probing catalytic active sites by DFT calculations

In order to unearth the insights into the role of graphene basal plane and structural defects, density functional theory (DFT) calculation was employed. In this study, since the interaction between ozone molecules and particular positions within graphene structure (basal plane, basal plane vacancy, armchair edge and zigzag edge) would be investigated, simplified pristine graphene models with different  $sp^2$  and  $sp^3$  carbon compositions from real graphene model were employed to simulate the adsorption effects with ozone molecules (Fig. 4). Previous studies reported the existence of different configurations of non-six-member rings as the vacancy sites inside graphene structure [43,44]. To simulate the structural vacancy, one carbon atom was removed from the graphene structure and the graphene model with vacancy sites was achieved by re-optimization of the remaining structure (Scheme S1). As seen, ozone molecule remains intact when placed above the graphene basal plane, yet the oxygen-oxygen bond length ( $l_{O-O}$ ) within the placed ozone molecule was slightly stretched from 1.286 to 1.316 Å (Table S4), suggesting the weak potential of activation of ozone molecule due to the free flowing electrons from  $sp^2$  carbon network, which is well agreement with the experimental observations. On the contrary, when the ozone molecule was located near the structural defects (vacancy and edges), the single-bonded oxygen atom spontaneously detaches from ozone structure and binds with the graphene plane to form a carbonyl group. Meanwhile, the remaining double-bonded oxygen atoms would drift away from the cluster to transfer into surface atom oxygen as potential ROS, which would be subsequently activated by an electron grabbing process. The adsorption energies of ozone on the vacancy, zigzag edge and armchair edge were calculated as  $-3.88$ ,  $-5.69$ , and  $-4.64$  eV, respectively, which were significantly lower than that bonded with graphene basal plane ( $-0.32$  eV). The stronger binding energy and newly formed active oxygen molecules indicate that the structural defects and edging sites are considerably more active than the intact graphene network for both ozone adsorption and decomposition. Therefore, edging sites might be envisaged with a higher catalytic potential in the real rGO/ozone system.

On the other hand, the surface oxygen functional groups on rGO are

also widely recognized as the critical active sites within carbocatalysis [41,42]. To evaluate the roles of oxygen functional groups on ozone decomposition, we modelled the different characterized functional groups (hydroxyl group, ketone group, carboxylic group and epoxy group) on the possible sites (basal plane, structural vacancies, zigzag/armchair edges) of graphene to investigate their impact on ozone molecule adsorption (Fig. S9). As seen in Table S5, the adsorption energy ozone molecule on different oxygen-containing groups of graphene models was much lower than those with structural defects, resulting in the structural completeness of ozone molecule. However, the  $l_{O-O}$  was obviously extended compared to that of free ozone molecule, indicating the potential of the activation to produce highly active ROS. Among different configurations, hydroxyl group on the zigzag edge of graphene (Fig. S9(B)) demonstrated the lowest adsorption energy with ozone and the largest  $l_{O-O}$ , suggesting the potential as the catalytic active sites. Hu et al. also proved that surface hydroxyls could serve as the Lewis acid sites for ozone adsorption and decomposition [4]. Meanwhile, the carbonyl groups (carboxyl and carbonyl group) with lone-pair electrons also displayed high tendency as the reactive sites for electron transfer during ozone decomposition process. Though the adsorption energy between ozone molecule and ketonic group was remarkably lower than that of carboxyl group, the prolonged  $l_{O-O}$  length also reveals the possibility for ozone decomposition on these sites. For epoxy group, a similar adsorption energy and  $l_{O-O}$  as those of graphene basal plane indicates a mediocre activation capability.

On the basis of above experimental and DFT calculation results, we postulate that structural defects (i.e. vacancies and defective edges) within rGO structure are the dominant active sites for ozone activation. The surface hydroxyl groups acting as the Lewis acid sites are favorable for ozone adsorption and decomposition, while the carbonyl groups accelerate the electron transfer process within the ozone activation.

### 3.4. Dominant ROS in catalytic ozonation of different organic pollutants

Previously, we found that the main ROS in catalytic ozonation of phenolics varied with the substituted groups [45]. To further probe the determination of target pollutants on the dominant ROS in catalytic ozonation, three aliphatic organics (OA, AA and FA) and three phenolic pollutants (4-NP, PHBA and ASA) were selected as the degradation targets for the radical scavenging tests (Fig. 5). Tert-butanol (t-BA) was employed as the  $\cdot OH$  quenching agent due to fast reaction rate with  $\cdot OH$  ( $(3.8-7.6) \times 10^8 \text{ M}^{-1} \text{ s}^{-1}$ ) and the inertness with ozone molecules ( $3 \times 10^{-5} \text{ M}^{-1} \text{ s}^{-1}$ ). For the three aliphatic organics, the addition of 12 mM of t-BA effectively quenched their degradation (Fig. 5(A-C)), suggesting that  $\cdot OH$  was the dominant ROS for the degradation of these aliphatic organics. In order to evaluate the reaction between  $\cdot OH$  and the aliphatic acids, the corresponding catalytic degradation curves were fitted with second order reaction kinetics (Fig. S10). The as calculated second order rate constant for catalytic degradation of OA, AA and FA was 0.10, 0.048 and  $0.040 \text{ min}^{-1}$ , respectively. The rate constant dropped with the decrease of molecular weight of the aliphatic acid, demonstrating that  $\cdot OH$  obtained high affinity towards the aliphatic acid with larger molecular weight. On the other hand, the presence of 12 mM of t-BA cannot show any quenching effect on 4-NP. Similar trends were observed for the other phenolic pollutants (Fig. 5(E-F)), indicating that  $\cdot OH$  was not the dominant ROS for destruction of these phenolics organics in the acid solution.

Sodium azide ( $\text{NaN}_3$ ) and p-benzoquinone (p-BQ) were also employed to evaluate the effects of  $^1\text{O}_2$  and  $\text{O}_2\cdot^-$  in catalytic ozonation of these organics, respectively [46,47]. Previous study revealed that addition of  $\text{NaN}_3$  in ozonated reaction solution under neutral or basic pH would result in formation of hypoazidite ( $\text{N}_3\text{O}^-$ ), a critical reaction intermediate accelerating the reaction between ozone molecules and azide [48]. In acidic solution, however, the sluggish reaction rate between  $\text{NaN}_3$  and  $\text{O}_3$  would hinder the formation of this metastable  $\text{N}_3\text{O}^-$  and thus prevent the further depletion of  $\text{O}_3$ . In order to evaluate

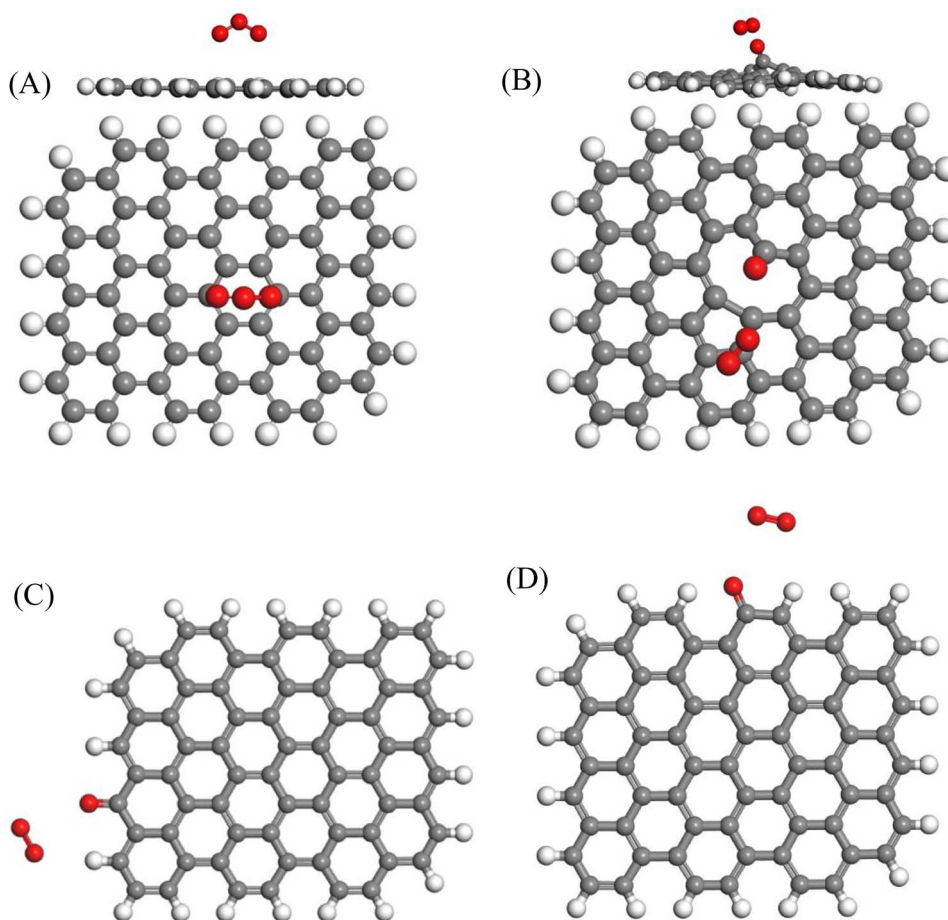


Fig. 4. DFT models of favorable adsorption structures of an ozone molecule on different sites of pristine graphene: (A) graphene basal plane, (B) vacancy, (C) zigzag edge and (D) armchair edge. The grey, white, and red atoms are C, H, and O atoms, respectively.

the influence of ozone molecules on sodium azide's quenching ability, control experiment for ozonation with 12 mM of sodium azide was carried out (Fig. S11). Under the acid condition (pH 3), the ozonation degradation curve of 4-NP with the addition of 12 mM  $\text{NaN}_3$  almost overlapped with the one without addition of  $\text{NaN}_3$ , suggesting that trivial reaction between ozone molecules and azide occurred in acid environment. Therefore,  $\text{NaN}_3$  could be employed as the quenching agent for singlet oxygen under acid condition. Apart from its high reaction rate towards  $^1\text{O}_2$  ( $2 \times 10^9 \text{ M}^{-1} \text{ s}^{-1}$ ),  $\text{NaN}_3$  also possessed strong scavenging effects against  $\cdot\text{OH}$  ( $1.2 \times 10^9 \text{ M}^{-1} \text{ s}^{-1}$ ) [49,50]. Since  $\cdot\text{OH}$  was proved as the dominant ROS for aliphatic pollutants degradation, addition of 12 mM  $\text{NaN}_3$  resulted in significant decrease in catalytic ozonation efficiency which was well in accordance with the TBA quenching results. For phenolic pollutants, the addition of  $\text{NaN}_3$  could evaluate the contribution of  $^1\text{O}_2$  towards pollutant degradation since TBA quench tests revealed that  $\cdot\text{OH}$  not responsible for phenolic pollutants degradation. The strong quenching effect of  $\text{NaN}_3$  (12 mM) indicates that  $^1\text{O}_2$  was one of the active species for these phenolic pollutants degradation. In the  $\text{O}_2\cdot^-$  scavenging tests with p-BQ, although p-BQ was partially consumed by ozone, the competition between it and the target pollutant was relatively insignificant and the remained was still adequate to scavenge  $\text{O}_2\cdot^-$  [8]. Fig. 5(D–F) showed that p-BQ effectively inhibited the degradation of the phenolic pollutants, and more than 65%, 50% and 40% of 4-NP, PHBA and ASA were remained, respectively. In light of these observations,  $\text{O}_2\cdot^-$  was postulated as another generated ROS responsible for phenolic pollutant degradation.

To further elucidate the domain reactive species in catalytic ozonation of phenolic and aliphatic pollutants, EPR was employed to identify the ROS utilizing DMPO, BMPO and TEMP as the spin-trapping

agents for detecting  $\cdot\text{OH}$ ,  $\text{O}_2\cdot^-$  and  $^1\text{O}_2$ , respectively (Fig. 6). EPR spectra of DMPO and BMPO and their response under the participation of  $\text{O}_3$  was shown in Fig. S13. Ultrapure water and absolute ethanol were employed as benchmark reaction matrix for measuring the possible ROS during LIB-rGO catalytic ozonation. Characteristic peaks for  $\cdot\text{OH}$ ,  $\text{O}_2\cdot^-$  and  $^1\text{O}_2$  were all detected when ultrapure water/ absolute ethanol were employed as the reaction matrix. Due to the fast reaction rate between the generated ROS and target organics, diluted organics solutions were employed as the sacrificing-scavengers for the produced ROS during EPR analysis. When 2 ppm of OA solution was employed as the reaction medium,  $\cdot\text{OH}$  radical signals with much lower intensities were identified (Fig. 6(A)), suggesting that most of the generated  $\cdot\text{OH}$  were consumed by OA molecules. The detection of strong signals for  $\text{O}_2\cdot^-$  and  $^1\text{O}_2$  indicates that  $\text{O}_2\cdot^-$  and  $^1\text{O}_2$  were produced during the catalytic ozonation process (Fig. 6(B–C)), yet previous studies also revealed that  $\text{O}_2\cdot^-$  and  $^1\text{O}_2$  cannot oxidize OA due to the low oxidation potential [51,52]. Therefore, it is most likely that OA was degraded by  $\cdot\text{OH}$ .

The situation differed when a diluted phenolic pollutant (4-NP) becoming the reaction medium. With the involvement of 2 ppm of 4-NP, no obvious characteristic peaks for  $\text{O}_2\cdot^-$  or  $^1\text{O}_2$  were discerned when BMPO and TEMP was employed as the spin trapping agents, respectively (Fig. 6(B–C)). These results suggested that the  $\text{O}_2\cdot^-$  and  $^1\text{O}_2$  radicals were possibly exhausted for 4-NP degradation, which was quite in agreement with the results of the radical scavenging tests (Fig. 5(D)). Interestingly, weak signals for  $\cdot\text{OH}$  radical were observed, suggested that  $\cdot\text{OH}$  radicals were either consumed for 4-NP decomposition or were merely generated with the presence of 4-NP. However, radical scavenging tests opposed the former speculation, indicating few  $\cdot\text{OH}$  radical was produced with the presence of 4-NP. Hence,  $\text{O}_2\cdot^-$  and  $^1\text{O}_2$



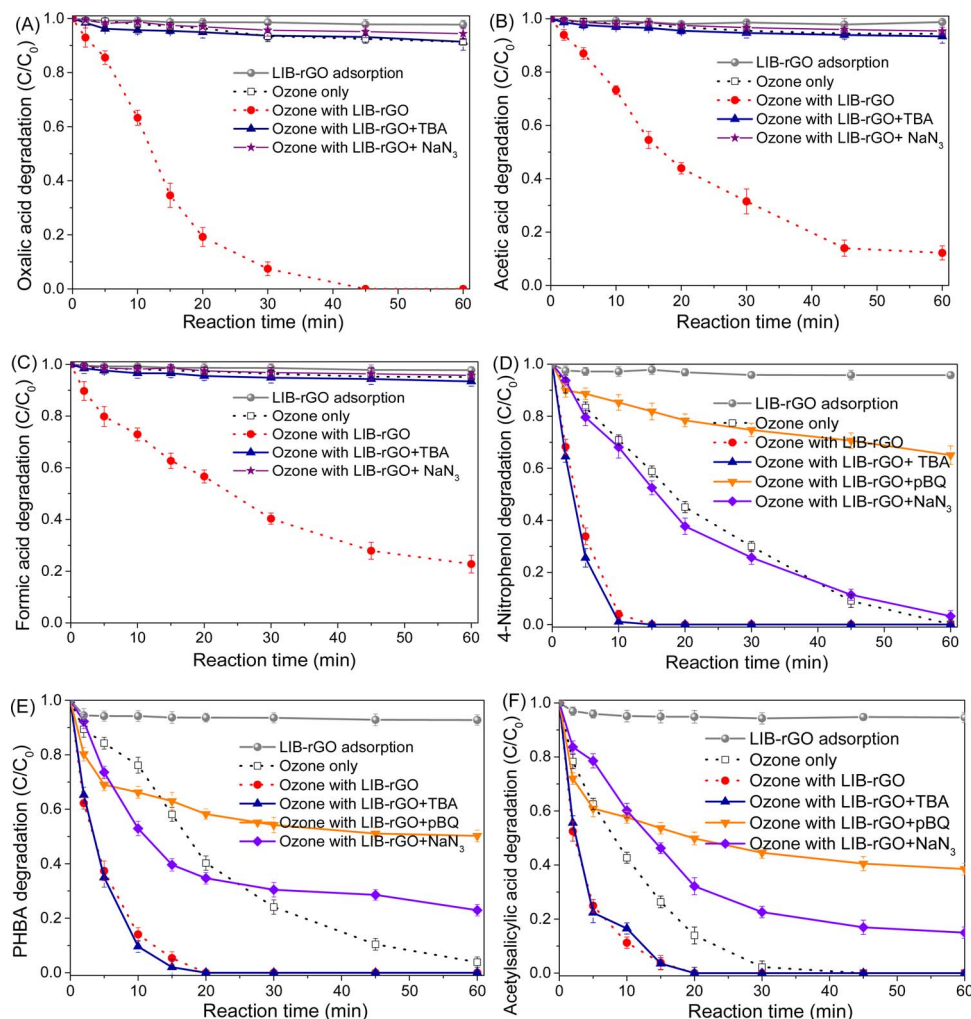
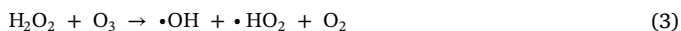
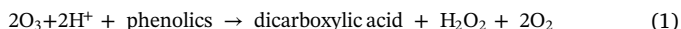


Fig. 5. Catalytic ozonation of OA (A), AA (B), FA acid (C), 4-nitrophenol (D), PHBA (E) and ASA (F) with different radical inhibitors. [Pollutant]<sub>0</sub>: 50 mg/L, Catalyst loading: 0.1 g/L, Ozone flow rate: 100 mL/min, Ozone concentration: 50 mg/L, Temperature: 25 °C. All initial pH was adjusted to 3.0.

radicals were the possible dominant ROS for 4-NP degradation.

### 3.5. Detection of H<sub>2</sub>O<sub>2</sub> production as oxidative intermediate species

As a stable intermediate for the generation of  $\cdot\text{OH}$ , H<sub>2</sub>O<sub>2</sub> is one of the vital reaction byproducts in ozonation/catalytic ozonation to quantify the  $\cdot\text{OH}$  production capability. The following equations (Eq. (1)–(4)) are possible production and evolution routes of H<sub>2</sub>O<sub>2</sub> in ozonation/catalytic ozonation system [53].



There are two pathways for H<sub>2</sub>O<sub>2</sub> generation in ozonation process. The first is the radical chain reactions in which H<sub>2</sub>O<sub>2</sub> is the chain termination product for  $\cdot\text{OH}/\text{HO}_2\cdot$  related radicals [54]. The second is the cycloaddition reaction between phenolic structure and ozone molecule to produce dicarboxylic acids and H<sub>2</sub>O<sub>2</sub> is byproduct in this process [55]. In an acidic solution, H<sub>2</sub>O<sub>2</sub> mainly existed in the form of molecule and its consumption by O<sub>3</sub> (Eq. (3)) is insignificant owing to the low reaction rate constant the reaction rate constant ( $< 0.01 \text{ M}^{-1}\text{s}$ ) [56]. In this study, to further investigate the as-discovered pollutant-dependent behavior, H<sub>2</sub>O<sub>2</sub> formation in ozonation and LIB-rGO catalytic ozonation

was detected by horseradish peroxidase method [57]. Moreover, the influence of the target pollutants on H<sub>2</sub>O<sub>2</sub> formation was also investigated (Fig. 7).

In ozonation experiments, ozone molecules seldom attacked OA actively and almost remained an inert status under pH 3.0. Therefore, trace amount of H<sub>2</sub>O<sub>2</sub> (less than 7  $\mu\text{M}$ ) was detected in ozonation of OA due to self-decomposition of ozone. In LIB-rGO catalytic ozonation, only around 2  $\mu\text{M}$  of H<sub>2</sub>O<sub>2</sub> was formed in the initial stage of the reaction (5 min). As  $\cdot\text{OH}$  was generated and acted as the dominant ROS for OA decomposition, we speculated that most of the generated  $\cdot\text{OH}$  were consumed by decomposing OA molecules, which also reflected by the sharp gradient of the degradation curve of OA in the first few minutes (Fig. 3(A)). Thus the chain termination reaction (Eq. (2)) merely happened. After 1 h of reaction, the concentration of H<sub>2</sub>O<sub>2</sub> in the solution increased to 6  $\mu\text{M}$ , which is rather close to that in ozonation. Within this period, OA in the solution have been destroyed and H<sub>2</sub>O<sub>2</sub> gradually accumulated to a steady value by chain termination reaction.

In terms of ozonation of 4-NP degradation, much more H<sub>2</sub>O<sub>2</sub> was generated compared with that in OA degradation. Since delocalized  $\pi$  electron within phenolic rings acted as a reactive center for direct ozone attack [58], H<sub>2</sub>O<sub>2</sub> formed as by-product in direct reaction between ozone and 4-NP (Eq. (1)). During the reaction, H<sub>2</sub>O<sub>2</sub> was gradually accumulated to achieve a steady concentration (27  $\mu\text{M}$ ). While in the LIB-rGO catalytic ozonation of 4-NP, part of 4-NP was oxidized by other active radicals, such as  $\text{O}_2\cdot^-$  and  $^1\text{O}_2$  which obtained higher redox potential than H<sub>2</sub>O<sub>2</sub>. This would reduce the ratio of direct ozone

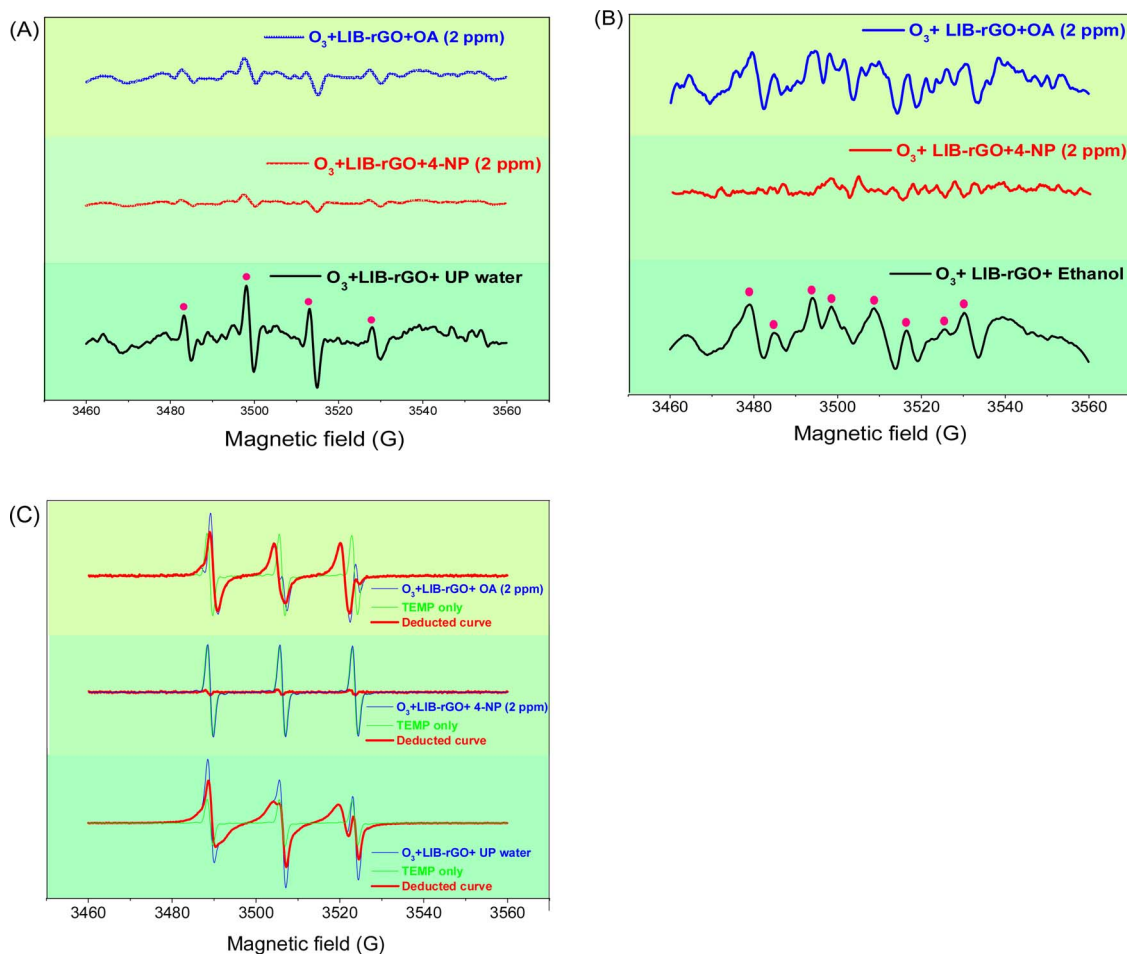


Fig. 6. (A) EPR spectra using DMPO as a trapping agent. (B) EPR spectra using BMPO as a trapping agent. Catalytic ozonation with BMPO was carried out in absolute ethanol. (C) EPR spectra using TEMP as a trapping agent. Catalyst loading: 0.2 g/L; ozone flow rate: 100 mL/min; ozone concentration: 5 mg/L; temperature: 25 °C.

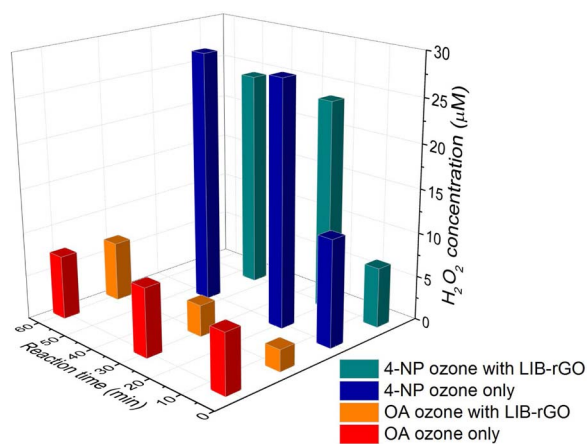


Fig. 7.  $H_2O_2$  production during ozonation and catalytic ozonation processes. [Target pollutant]<sub>0</sub>: 50 mg/L, Catalyst loading: 0.1 g/L, Ozone flow rate: 100 mL/min, Ozone concentration: 50 mg/L, Temperature: 25 °C.

oxidation, and thus lower concentration of  $H_2O_2$  was detected in the LIB-rGO catalytic process than that in ozonation.

### 3.6. Effect of phosphate anions

Gaseous ozone molecules prefer to dissociate to yield a surface oxygen atom or some reactive species on strong Lewis acid sites of the catalysts [59] or coordinate with weak Lewis acid sites via one of the

terminal oxygen atoms [60]. In aqueous phases, however, these processes cannot be confirmed because of the existence of strong Lewis bases. To investigate the role of catalyst surface properties in catalytic ozonation over aliphatic and phenolic pollutants, sodium triphosphate (5 mM) was added both in catalytic ozonation of OA and 4-NP owing to strong bonding effect between phosphate and the Lewis acid sites of the catalyst [20].

With the presence of phosphate (5 mM), catalytic ozonation over OA was greatly inhibited (Fig. 8(A)). As seen, only 20% of the initial OA was degraded after 60 min of the reaction. As discussed above, defects among the graphene structure are the potential active sites for catalytic ozonation. Some carbon atoms within the defects structures including vacancies within the graphene basal structural and the zigzag/armchair edge possess strong positive charges which are strong Lewis acid sites for accepting electrons, while others were negatively charged acting as Lewis bases [61]. Phosphate anions could displace the adsorbed OA molecules and might also compete for the surface active sites with ozone molecules. On one hand, phosphate anions replaced the ozone molecules and adsorbed on the positive-charged carbon atoms within the defects which disabled their catalytic activities. On the other hand, ozone molecules might decompose at the defect sites to generate hydroxyl radicals, which were also strong Lewis acid sites. Before the hydroxyl radicals were released to the bulk solution, phosphate acted as the radical scavenger to instantaneously bond with them and thus quenched the reaction. Whatever the possible route is, the decomposition of OA molecules occurred on the surface of the catalyst.

Catalytic ozonation over the phenolic pollutant demonstrated the opposite scenario (Fig. 8(B)). Addition of phosphate did not bring



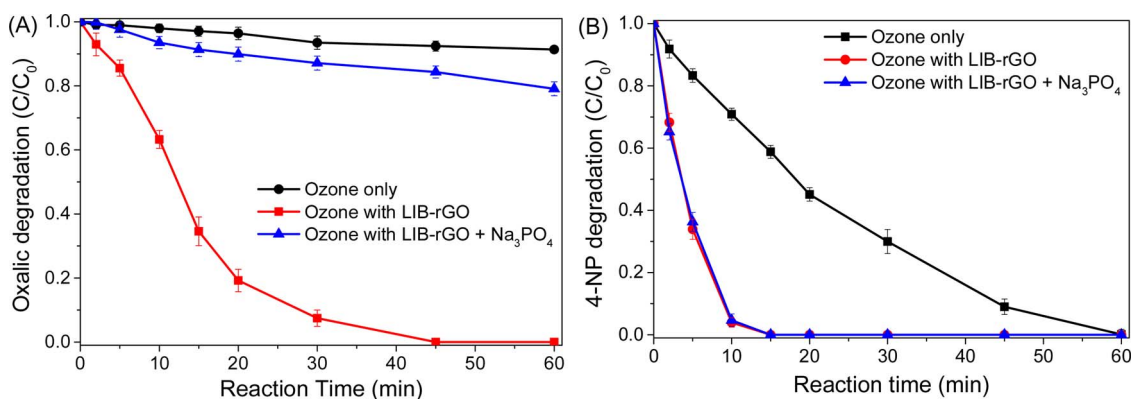


Fig. 8. Effect of phosphate on the degradation of OA (A) and 4-NP (B) in different ozone aqueous solution. [OA]<sub>0</sub>: 50 mg/L, [4-NP]<sub>0</sub>: 50 mg/L, Catalyst loading: 0.1 g/L, Ozone flow rate: 100 mL/min, Ozone concentration: 50 mg/L, Temperature: 25 °C; [Na<sub>3</sub>PO<sub>4</sub>] = 5 mM.

negative effect against 4-NP degradation, the resulted degradation curve almost overlapped the original one. In this case, although the Lewis acids sites were blocked by phosphate anions, ozone molecules would actively attack phenolic pollutants and tend to be transformed into H<sub>2</sub>O<sub>2</sub>. It is plausible that negatively charged carbon atoms and the oxygen-contained functional groups might transfer electrons for H<sub>2</sub>O<sub>2</sub> formation and responsible for activating O<sub>3</sub> molecules and the formed H<sub>2</sub>O<sub>2</sub> into ROS (superoxide radicals and singlet oxygen). And 4-NP degradation occurred in bulk solution. However, the detailed mechanism for these electron transfer and activation processes still remain to be unraveled.

In light of these results, the dominant ROS differed with respect to the types of target pollutants in LIB-rGO catalyzed ozonation. For the aliphatic pollutants being hardly directly attacked by ozone molecule, ozone was decomposed over the catalysts to produce  $\cdot\text{OH}$  radicals, via which the pollutants were degraded. For the phenolic pollutants easily attacked by ozone, they were oxidized by ozone molecule and other species ( $\text{O}_2\cdot^-$  and  $^1\text{O}_2$ ). Superoxide radical could act as the bridge for the formation of hydroxyl radical in catalytic ozonation [51,62]. EPR and radical quenching tests revealed that  $\text{O}_2\cdot^-$  was an important radical for phenols degradation, however, its transformation to  $\cdot\text{OH}$  was possibly greatly inhibited by the presence of the phenols. When aliphatic acids were employed as the target pollutants,  $\cdot\text{OH}$  became the dominant ROS owing to the transformation of  $\text{O}_2\cdot^-$ . Therefore, both  $\text{O}_2\cdot^-$  and  $\cdot\text{OH}$  could be produced in catalytic ozonation in the same condition, yet their ratios or evolution might be greatly influenced by the organics in the solution. Certain amount of H<sub>2</sub>O<sub>2</sub> was produced during direct attack of ozone molecule, but its relatively low redox potential limited further destruction of the intermediates [63]. In this study, however, due to the fast reaction rate and the transitional feature, hydroperoxy radical ( $\cdot\text{HO}_2$ ) was unable to identify. Further efforts are still required to capture and identify the existence of the intermediate  $\cdot\text{HO}_2$ .

### 3.7. Stability and reusability of LIB-rGO

A four-cycle successive test was performed to evaluate the stability and recyclability of the LIB-rGO towards 4-NP degradation wherein the catalyst was collected by vacuum filtration, washed with ultrapure water for 3 times and dried in a 80 °C oven before use (Fig. 9). As seen, the passivation process occurred to the LIB-rGO with the increase of reuse time. In the 4th run, complete 4-NP degradation was postponed from 15 min to 60 min, and the corresponding TOC removal rate was decreased from 92% to 62% (Fig. 9(B)). However, compared with the ozonation (23% TOC removal rate), the used LIB-rGO catalyst still demonstrated a strong catalytic ozonation activity. Our previous studies revealed that the deactivation of the carbon catalysts such as rGO and MWCNTs mainly derived from the changes of surface chemistry and the

coverage of the active sites by degradation intermediates [8,64]. Owing to the strong oxidation abilities of ozone molecules and the generated ROS, part of the surface hydroxyl groups which obtained the high catalytic potential for stretching I<sub>O-O</sub> with ozone molecule would be oxidized to carbonyl or carboxylic groups possessing the lower catalytic activities [8]. Moreover, the structural defects might be blocked by the degradation intermediates and thus leading to a decrease of the specific surface area and pore volume [5,64]. Nevertheless, the catalytic activity of the carbon catalysts could be recovered by a mild heat treatment [34].

## 4. Conclusions

In summary, a graphite from spent LIBs anode was reused to synthesize a series of graphene-based materials for catalytic ozonation of organic pollutants. Raman analysis and degradation results illustrated that higher defective level of LIB-rGO were responsible for the greater catalytic potential. DFT calculation provided in-depth evidence that defect sites within graphene structure were the dominant active sites for ozone decomposition, and surface oxygen-containing groups also contributed to ozone decomposition by O–O bond stretching. Radical scavenging tests and EPR results revealed that the dominant ROS varied upon the structure of organic pollutants.  $\cdot\text{OH}$  was identified as the dominant ROS for the aliphatic pollutants (OA, AA and FA) degradation, while ozone,  $\text{O}_2\cdot^-$  and  $^1\text{O}_2$  were responsible for the destruction of the phenolic pollutants (PHBA, 4-NP and ASA). These results not only facilitate insights into the contribution of structural defects in graphene-based materials catalytic ozonation, but also envisage a comprehensive understanding of the relationship between the structures of the target pollutants and the dominant ROS.

## Acknowledgements

The authors greatly appreciate the financial supports from the National Science Fund for Distinguished Young Scholars of China (No. 51425405), the National Natural Science Foundation of China (No. 21606253), Science Foundation of China University of Petroleum, Beijing (No. 2462016YJRC013) and Beijing Natural Science Foundation (8172043).

## Appendix A. Supplementary data

Supplementary data associated with this article including XRD patterns of the catalysts, XPS spectra, TG analysis, and variation of oxalic acid concentration/ozone concentration/catalysts loading during the experiments, kinetic studies, DFT modeling, TOC removal profiles and EPR spectra can be found, in the online version, at doi:<https://doi.org/10.1016/j.apcatb.2018.02.010>.

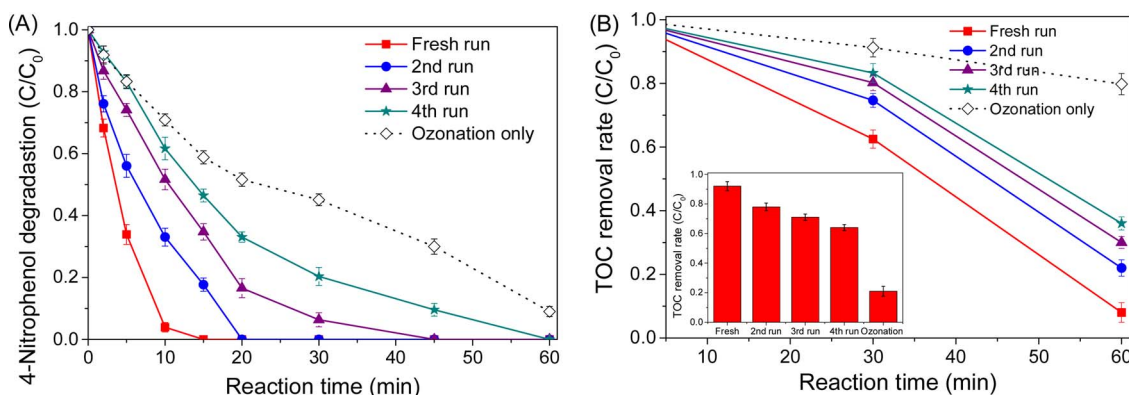


Fig. 9. Successive reusability test for 4-nitrophenol degradation (A) and the corresponding TOC removal profiles and rate (inset) (B). Reaction conditions: [4-nitrophenol]<sub>0</sub> = 50 mg/L, Catalyst loading = 0.1 g/L, Ozone flow rate: 100 mL/min, Ozone loading: 50 mg/L, Temperature: 25 °C, All initial pH was adjusted to 3.0.

## References

- [1] J.L. Schnoor, *Environ. Sci. Technol.* 45 (2011) 5065.
- [2] E. Saputra, S. Muhammad, H. Sun, H.M. Ang, M.O. Tade, S. Wang, *Environ. Sci. Technol.* 47 (2013) 5882–5887.
- [3] Y. Zhou, J. Jiang, Y. Gao, J. Ma, S. Pang, J. Li, X. Lu, L. Yuan, *Environ. Sci. Technol.* 49 (2015) 12941–12950.
- [4] J. Bing, C. Hu, Y. Nie, M. Yang, J. Qu, *Environ. Sci. Technol.* 49 (2015) 1690–1697.
- [5] X. Duan, H. Sun, J. Kang, Y. Wang, S. Indrawirawan, S. Wang, *ACS Catal.* 5 (2015) 4629–4636.
- [6] H. Sun, S. Liu, G. Zhou, H.M. Ang, M.O. Tade, S. Wang, *ACS Appl. Mater. Interfaces* 4 (2012) 5466–5471.
- [7] P. Liang, C. Zhang, X. Duan, H. Sun, S. Liu, M.O. Tade, S. Wang, *Environ. Sci. Nano* 4 (2017) 315–324.
- [8] Y. Wang, Y. Xie, H. Sun, J. Xiao, H. Cao, S. Wang, *ACS Appl. Mater. Interfaces* 8 (2016) 9710–9720.
- [9] A. Ikhtlaq, D.R. Brown, B. Kasprzyk-Hordern, *Appl. Catal., B* 129 (2013) 437–449.
- [10] F. Nawaz, Y. Xie, H. Cao, J. Xiao, Y. Wang, X. Zhang, M. Li, F. Duan, *Catal. Today* 258 (Part 2) (2015) 595–601.
- [11] M.M. Titirici, R.J. White, N. Brun, V.L. Budarin, D. Su, F. del Monte, J.H. Clark, M.J. MacLachlan, *Chem. Soc. Rev.* 44 (2015) 250–290.
- [12] D. Su, S. Perathoner, G. Centi, *Chem. Rev.* 113 (2013) 5782–5816.
- [13] Z. Li, Z. Liu, H. Sun, C. Gao, *Chem. Rev.* 115 (2015) 7046–7117.
- [14] S.N. Stamatina, I. Hussainova, R. Ivanov, P.E. Colavita, *ACS Catal.* 6 (2016) 5215–5221.
- [15] Z. Liu, J. Ma, Y. Cui, L. Zhao, B. Zhang, *Appl. Catal., B* 101 (2010) 74–80.
- [16] J. Liu, Z. Chen, Q. Wu, A. Li, H. Hu, C. Yang, *Sci. Rep.* 6 (2016) 31405.
- [17] F. Nawaz, H. Cao, Y. Xie, J. Xiao, Y. Chen, Z.A. Ghazi, *Chemosphere* 168 (2017) 1457–1466.
- [18] Z. Liu, J. Ma, Y. Cui, B. Zhang, *Appl. Catal., B* 92 (2009) 301–306.
- [19] Y. Wang, Y. Xie, H. Sun, J. Xiao, H. Cao, S. Wang, *Catal. Sci. Technol.* 6 (2016) 2918–2929.
- [20] A. Lv, C. Hu, Y. Nie, J. Qu, *Appl. Catal., B* 117 (2012) 246–252.
- [21] Q. Ma, Y. Yu, M. Sindoro, A.G. Fane, R. Wang, H. Zhang, *Adv. Mater.* 29 (2017) N/a–N/a.
- [22] W. Zhang, W. Lai, R. Cao, *Chem. Rev.* 117 (2017) 3717–3797.
- [23] R.M. Navarro, M.A. Peña, J.L.G. Fierro, *Chem. Rev.* 107 (2007) 3952–3991.
- [24] L. Liu, X. Yang, N. Ma, H. Liu, Y. Xia, C. Chen, D. Yang, X. Yao, *Small* 12 (2016) 1295–1301.
- [25] P. Chen, L. Wang, G. Wang, M. Gao, J. Ge, W. Yuan, Y. Shen, A. Xie, S. Yu, *Energy Environ. Sci.* 7 (2014) 4095–4103.
- [26] Z. Wu, C. Li, H. Liang, J. Chen, S. Yu, *Angew. Chem. Int. Ed.* 52 (2013) 2925–2929.
- [27] S. Chen, G. He, H. Hu, S. Jin, Y. Zhou, Y. He, S. He, F. Zhao, H. Hou, *Energy Environ. Sci.* 6 (2013) 2435–2439.
- [28] S. Natarajan, D. Shanthana Lakshmi, H.C. Bajaj, D.N. Srivastava, *J. Environ. Chem. Eng.* 3 (2015) 2538–2545.
- [29] O.A. Ogunseitan, J.M. Schoenung, J.-D.M. Saphores, A.A. Shapiro, *Science* 326 (2009) 670–671.
- [30] W.S. Hummers, R.E. Offeman, *J. Am. Chem. Soc.* 80 (1958) 1339.
- [31] S. Stankovich, D.A. Dikin, R.D. Piner, K.A. Kohlhaas, A. Kleinhammes, Y. Jia, Y. Wu, S.T. Nguyen, R.S. Ruoff, *Carbon* 45 (2007) 1558–1565.
- [32] A. Chakravarty, D. Sengupta, B. Basu, A. Mukherjee, G. De, *RSC Adv.* 5 (2015) 92585–92595.
- [33] S.M. Badawy, *Environ. Prog. Sustain. Energy* 35 (2016) 1485–1491.
- [34] H. Sun, Y. Wang, S. Liu, L. Ge, L. Wang, Z. Zhu, S. Wang, *Chem. Commun.* 49 (2013) 9914–9916.
- [35] X. Duan, Z. Ao, L. Zhou, H. Sun, G. Wang, S. Wang, *Appl. Catal. B* 188 (2016) 98–105.
- [36] F.J. Beltrán, F.J. Rivas, R. Montero-de-Espinoza, *Appl. Catal. B* 39 (2002) 221–231.
- [37] J. Xiao, Y. Xie, H. Cao, Y. Wang, Z. Guo, Y. Chen, *Carbon* 107 (2016) 658–666.
- [38] Y. Wang, Z. Ao, H. Sun, X. Duan, S. Wang, *Appl. Catal. B* 198 (2016) 295–302.
- [39] J. Kim, A.J. Page, S. Irle, K. Morokuma, *J. Am. Chem. Soc.* 134 (2012) 9311–9319.
- [40] C. Chen, C.T. Jafvert, *Environ. Sci. Technol.* 44 (2010) 6674–6679.
- [41] J. Zhang, D. Su, R. Blume, R. Schlögl, R. Wang, X. Yang, A. Gajović, *Angew. Chem. Int. Ed.* 49 (2010) 8640–8644.
- [42] V.N. Mochalin, O. Shenderova, D. Ho, Y. Gogotsi, *Nat. Nanotechnol.* 7 (2012) 11–23.
- [43] O. Lehtinen, S. Kurasch, A.V. Krashenninnikov, U. Kaiser, *Nat. Commun.* 4 (2013) 2098.
- [44] W. Li, M. Zhao, X. Zhao, Y. Xia, Y. Mu, *Phys. Chem. Chem. Phys.* 12 (2010) 13699–13706.
- [45] F. Nawaz, Y. Xie, J. Xiao, H. Cao, Z.A. Ghazi, Z. Guo, Y. Chen, *Catal. Sci. Technol.* 6 (2016) 7875–7884.
- [46] J. Catalán, C. Díaz, L. Barrio, *Chem. Phys.* 300 (2004) 33–39.
- [47] A. Jawad, X. Lu, Z. Chen, G. Yin, *J. Phys. Chem. A* 118 (2014) 10028–10035.
- [48] E.A. Betterton, D. Craig, *J. Air Waste Manage. Assoc.* 49 (1999) 1347–1354.
- [49] N. Hasty, P.B. Merkel, P. Radlick, D.R. Kearns, *Tetrahedron Lett.* 13 (1972) 49–52.
- [50] K. Ogino, N. Kodama, M. Nakajima, A. Yamada, H. Nakamura, H. Nagase, D. Sadamitsu, T. Maekawa, *Free Radic. Res.* 35 (2001) 735–747.
- [51] J. Xiao, J. Rabeah, J. Yang, Y. Xie, H. Cao, A. Brückner, *ACS Catal.* 7 (2017) 6198–6206.
- [52] J. Xiao, Y. Xie, F. Nawaz, S. Jin, F. Duan, M. Li, H. Cao, *Appl. Catal. B* 181 (2016) 420–428.
- [53] S. Afzal, X. Quan, J. Zhang, *Appl. Catal. B* 206 (2017) 692–703.
- [54] B. Kasprzyk-Hordern, M. Ziółek, J. Nawrocki, *Appl. Catal. B* 46 (2003) 639–669.
- [55] Y. Yamamoto, E. Niki, H. Shiokawa, Y. Kamiya, *J. Org. Chem.* 44 (1979) 2137–2142.
- [56] T.M. Lesko, A.J. Colussi, M.R. Hoffmann, *J. Am. Chem. Soc.* 126 (2004) 4432–4436.
- [57] L.A. Sternberger, P.H. Hardy, J.J. Cuculis, H.G. Meyer, *J. Histochem. Cytochem.* 18 (1970) 315–333.
- [58] J. Rivera-Utrilla, M. Sánchez-Polo, *Appl. Catal. B* 39 (2002) 319–329.
- [59] R. Radhakrishnan, S.T. Oyama, *J. Catal.* 204 (2001) 516–519.
- [60] K.M. Bulatin, J.C. Lavalley, A.A. Tsyganenko, *J. Phys. Chem.* 99 (1995) 10294–10298.
- [61] L. Zhang, Q. Xu, J. Niu, Z. Xia, *Phys. Chem. Chem. Phys.* 17 (2015) 16733–16743.
- [62] J. Staehelin, J. Hoigne, *Environ. Sci. Technol.* 19 (1985) 1206–1213.
- [63] B. Legube, N. Karpel Vel Leitner, *Catal. Today* 53 (1999) 61–72.
- [64] X. Duan, H. Sun, Y. Wang, J. Kang, S. Wang, *ACS Catal.* 5 (2015) 553–559.